



Long eye relief fundus camera and fixation target with partial correction of ocular longitudinal chromatic aberration

SAMUEL STEVEN,^{1,2} YUSUFU N. SULAI,^{3,4} SOON K. CHEONG,² JULIE BENTLEY,¹ AND ALFREDO DUBRA^{2,*}

¹*Institute of Optics, University of Rochester, Rochester, NY 14620, USA*

²*Department of Ophthalmology, Stanford University, Palo Alto, CA 94303, USA*

³*Department of Ophthalmology, Medical College of Wisconsin, Milwaukee, WI 53226, USA*

⁴*Currently at Facebook Reality Labs Redmond, WA 98052, USA*

*adubra@stanford.edu

Abstract: A combined 32° full field of view refractive fundus camera and fixation target with a −20 to +10 diopter sphere correction range is described and demonstrated. The optical setup partially corrects the average longitudinal chromatic aberration and spherical aberration of the human eye, while providing a long eye relief to allow integration with reflective adaptive optics ophthalmoscopes, as a viewfinder. The fundus camera operates with 940 nm light, using a maximum 2.9 mm diameter imaging pupil at the eye. The fixation target uses a light projector capable of delivering red, green and/or blue spatially and temporally modulated stimuli to the retina. The design and performance of each sub-system are discussed, and retinal imaging at various wavelengths is demonstrated.

© 2018 Optical Society of America under the terms of the [OSA Open Access Publishing Agreement](#)

1. Introduction

Current high-resolution adaptive optics (AO) ophthalmoscopes have a 1-3° field of view (FOV) [1–14], due to the size of the isoplanatic angle of the human eye which varies across individuals and with pupil diameter [15,16]. Steering such a small FOV to the retinal region of interest using just a live image from the AO ophthalmoscope itself presents important practical challenges due to involuntary eye motion and retinal pathology. Various solutions have been proposed and demonstrated to address this problem, including the use of a wide-field ophthalmoscope with an AO scanning light ophthalmoscope (AOSLO) [17–19], or by temporarily increasing the AO ophthalmoscope's FOV [20]. Fixation targets have also been demonstrated and whether internal [1,21–24] or external [2,8,25–32], are only a partial solution in that they do not address changes in fixation locus due to disease. Here, we propose an instrument that combines an internal fixation target with a near infrared fundus camera as a viewfinder. In addition to assisting and validating the fixation steering, and by allowing a small fraction of the AO ophthalmoscope light to reach the camera [17], the fundus pictures provide an accurate record of the AO ophthalmoscope FOV location. This will in turn facilitate the montaging of AO retinal images, which is a well-recognized problem [33–35] and currently a challenge for longitudinal imaging. The instrument was designed with an unusually long eye relief to allow integration with reflective adaptive optics ophthalmoscopes. Both the fixation and imaging arms of the instrument partially correct the longitudinal chromatic aberration (LCA) [36–40] and spherical aberration [41–43] of the average human eye.

In what follows we outline the system specifications and first order layout of the full optical system. Next, a description of the design of each of the instrument's subsystems, including optical and mechanical tolerance analysis is provided. Finally, we demonstrate the

assembled and fully functional instrument, and include the measurement of various performance metrics.

2. Instrument design

2.1 System specifications

The proposed instrument was specified to provide a fundus view and steerable fixation over a 30° FOV, with a spectacle sphere correction range of -20 to +10 diopters (D). This focus range covers the majority of the human population [44–47], and is achieved through the use of a Badal optometer configuration [48]. The fundus camera will operate in reflectance at 940 nm to allow functional AO retinal imaging experiments by avoiding photoreceptor stimulation (photopic spectral luminous efficiency function V at 940 nm is smaller than 10⁻⁶ ([49]), as well as overlap with the potentially broad spectrum (400-900 nm) of most AO ophthalmoscopes [8]. The visual target must be able to display red, green and/or blue images to direct the fixation of subjects with any color vision deficiency. This fixation channel could also be used to deliver spatially and/or temporally modulated light stimuli to the retina in order to elicit functional changes such as photoreceptor reflectivity fluctuations [31, 50, 51] or blood vessel lumen changes [52–55]. The optical path of the proposed instrument and the AO ophthalmoscope were combined through a dichroic beam splitter between the eye and their corresponding first optical elements, providing a minimum eye relief of 90 mm. The optics were designed to correct for the average spherical aberration (0.138 μm Zernike spherical over a 5.7 mm pupil [42]) and LCA (1.09 D from 455-625 nm [38] and 0.02D from 920-960 nm [39]) of the human eye, aiming to achieve a theoretical diffraction-limited ($\lambda/14$) root-mean-squared (RMS) wavefront, across the entire FOV, and $\lambda/10$ after assembly. The fundus camera will image the retina through a maximum 2.9 mm diameter pupil at the eye in order to balance light collection efficiency and spatial resolution set by diffraction and ocular monochromatic aberrations [56, 57]. The major specifications, including those discussed above, are listed in Table 1 below.

Table 1. Fundus camera and fixation target design specifications

Specification	Value
Full field of view	$\geq 30^\circ$ of visual angle
Eye relief	≥ 90 mm
Sphere prescription range	-20 to +10 D
Focusing method	Afocal (Badal) zoom relay
Spectral bandwidth	Fixation/stimulation: 455 - 625 nm Fundus imaging: 920 - 960 nm
Design performance	$< \lambda/14$ RMS wavefront for all field angles & wavelengths
As-built performance	$< \lambda/10$ RMS wavefront for all field angles & wavelengths
Spherical aberration correction	0.138 μm (Zernike spherical) over a 5.7 mm pupil [42]*
Longitudinal chromatic aberration	1.09 D (455-625 nm) [38], 0.02 D (920-960 nm) [39]

* Porter et al. [42] followed 'OSA standard for reporting the optical aberrations of eyes' [58], which uses Zernike polynomials normalized over the unit circle area. Code V (Synopsys Inc., Mountain View, CA, USA), uses a different normalization, which requires the following scaling: $\{z_i^c\}_{\text{OSA}} = \sqrt{5} \{z_i^c\}_{\text{Code V}}$.

2.2 First order design

The first order schematic of the full optical system is shown below in Fig. 1. The fundus camera, illumination and fixation arms, as well as the transmission curves for custom dichroic mirrors D_1 , D_2 and D_3 (Omega Optical, Brattleboro, Vermont, USA) are arranged to prioritize light safety (see Appendix A for maximum permissible exposure calculations). Dichroic mirrors 1 and 3 have the same transmission curves, in which light of 910-980 nm wavelengths and the 450-850 nm range are $> 90\%$ reflected and transmitted, respectively, in both s- and p-polarizations. The second dichroic reflects more than 90 and 50% of s-polarized light in the

910-980 nm and 450-650 nm ranges, respectively, with a polarization ratio of ~ 5 and ~ 2 , respectively, to mitigate corneal and internal optics reflections. The combination of dichroic elements allows a small fraction of the AO ophthalmoscope imaging light to be diverted to the fundus camera, revealing the location of the AO ophthalmoscope's FOV in reference to the larger FOV of the fundus image as shown later (section 3.2). The illumination path is placed after the afocal relay to provide constant illumination at the eye, irrespective of the focus.

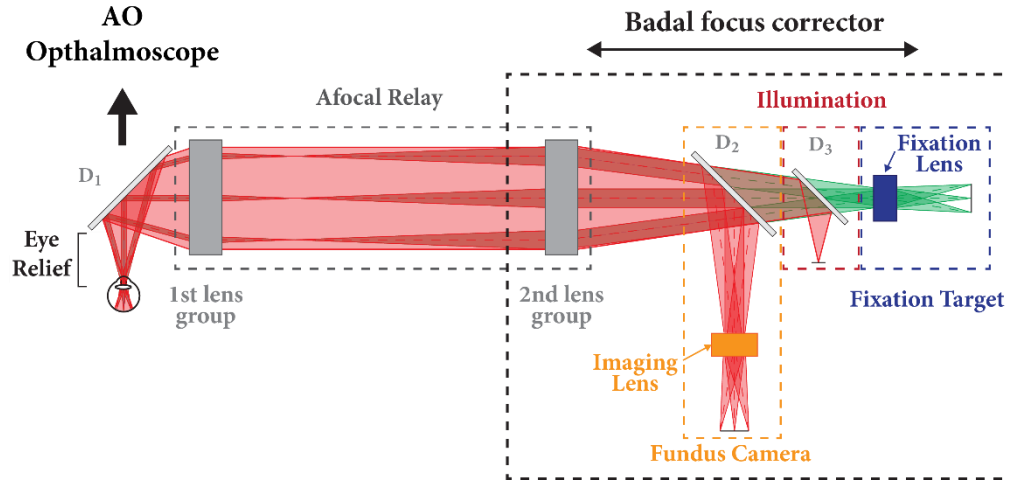


Fig. 1. Near infrared fundus camera and fixation target optical layout (D_1 , D_2 and D_3 are dichroic mirrors).

2.3 Optical design optimization

The optical design was optimized using Code V, modeling the ocular aberrations as a paraxial lens that induces only the average LCA, transverse chromatic aberration (TCA), and spherical aberration for the human eye (see Table 1). The conversion of published numbers to waves is as follows. The dioptric power φ_d at the pupil of the eye is related to a marginal ray angle u'_a , through paraxial ray tracing: $u'_a = -\varphi_d y_p$, where y_p is the pupil radius. To convert from this marginal ray angle to waves of defocus, the wavefront ($W = W_{020} \rho^2$) derivative must be evaluated at the edge of the pupil ($\rho = 1$) and scaled by the pupil size,

$$u'_a = 2W_{020} / y_p,$$

which solving for W_{020} in units of waves yields

$$W_{020} = -\frac{\varphi_d y_p^2}{2\lambda}.$$

Spherical aberration was modeled by adding a surface in the entrance pupil of the paraxial lens defined as a fringe Zernike polynomial with a normalization radius of 2.85 mm (see Table 1).

2.4 Fundus camera illumination

A ring of five 940 nm light-emitting diodes (LEDs) SMBB940DS-1100-02 (Marubeni, Tokyo, Japan) was custom made to illuminate the retina uniformly within the required 30° FOV. This LED ring is optically conjugate to the pupil of the eye and has a sufficiently large radius (see Fig. 2) to avoid overlap with the pupil of the imaging arm, as is commonly done in fundus cameras to mitigate corneal and internal optics back reflections [59–61]. To further

mitigate these undesired back reflections, a linear polarizer was placed after the LEDs (LPVIS100, Thorlabs Inc., Newton, New Jersey, U.S.A.), with an identical but orthogonal linear polarizer placed in front of the imaging sensor. The extinction ratio of these crossed-polarizers was increased by the polarization-dependent custom dichroic D₂ shown in Fig. 1.

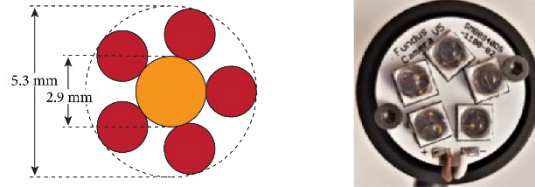


Fig. 2. Custom LED ring as seen at the pupil of the eye (left) and as built on a heatsink (Thorlabs, MXXXL1-SP; right). The red circles represent the LEDs and the orange circle the imaging pupil.

2.5 Afocal relay

The afocal relay (Fig. 1), is comprised of two lens groups that relay the pupil of the eye to an accessible conjugate plane. Correction of the sphere component of the spectacle prescription and retinal focusing are achieved by translating the entire instrument along the optical axis relative to the first lens group, which remains at a fixed distance from the eye. The first lens group is placed a focal length away from the eye to force telecentricity, thus preventing a change in the retinal magnification during focusing (as in a Badal optometer). This approach also assures that the exit pupil of the afocal relay remains at a fixed distance from the second lens group. The specifications for the afocal relay are shown below in Table 2, with the field of view, eye relief and telecentricity requirements dictating that the optical elements of the first and second groups must have a minimum of 50 mm clear aperture. The focal length of each group was dictated based on the mechanical limitations imposed by the required eye relief as well as the beam splitters for integrating the illumination and imaging subsystems (see Fig. 1). In order to reduce cost, these large elements were chosen to be off-the-shelf doublets.

Table 2. Afocal relay specifications

Specification	Value
Aperture stop diameter	2.9 mm at the eye
Full field of view	$\geq 30^\circ$ of visual angle
Afocal magnification	2.6
Spectral bandwidth	455-625 nm (fixation) and 920-960 nm (imaging)
Eye relief	≥ 90 mm
Ocular focusing method	Afocal zoom relay – one moving group
Surface types	Refractive & spherical
Overall size	$< 80 \times 7.6 \times 7.6$ cm
Performance of all field angles & wavelengths	$< \lambda/14$ RMS wavefront at 0 D $< \lambda/10$ RMS wavefront from +10 to -20 D
Ocular aberration correction	LCA: 1.09 D (455-625 nm) & 0.02 D (920-960 nm) Spherical aberration: 0.138 μ m Zernike over a 5.7 mm pupil

Each lens group consists of two achromatic doublets (Ross Optical: L-AOC288/220, L-AOC295/220 & L-AOC300/220, which in Fig. 3 are E1, E2 and E3, respectively) with their orientation optimized to minimize spherical aberration. The performance of the system was evaluated by placing a paraxial lens in the exit pupil of the afocal relay, with the focal length (fundus camera: 46.6 mm & fixation: 17.9 mm) that would provide the required image size on the fundus camera sensor and the projector digital micro-mirror device (DMD). When the system is evaluated in this manner, the afocal relay is limited by field curvature, while in the fixation channel, LCA and TCA are the limiting aberrations, shown in Fig. 3(b)-(e). In what

follows, we assume that the TCA for the fixation target can be corrected digitally by scaling each of the color channels in the DLP projector using theoretically-derived or experimental TCA values. The maximum polychromatic RMS wavefront (as per Code V's definition) was 0.066 waves for the fundus camera ($\lambda/15$), and, when considering the monochromatic aberrations for the fixation target wavelengths, the RMS wavefront was 0.038 ($\lambda/26$) waves..

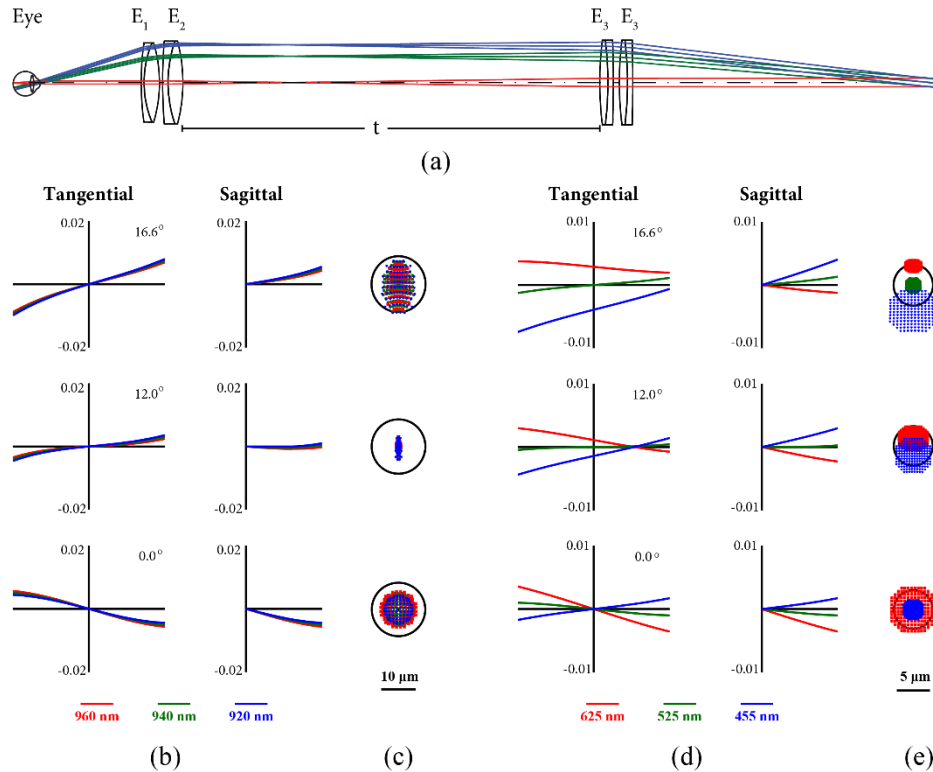


Fig. 3. Afocal relay optics layout (a), in which the distance t between the lens groups can be set to 272, 399 and 524 mm for correcting -10 , 0 and $+10$ D of sphere, respectively. Transverse ray aberration curves over normalized pupil coordinates (b, d), in units of mm. Spot diagrams (c, e), in which the black circles represent the Airy disk at the central wavelengths of each range (940 & 525 nm, respectively). All diagrams correspond to 0 D of defocus.

2.6 Fundus camera objective

The fundus camera objective specifications are derived from those of the full instrument, afocal relay (Table 3), and camera (Grasshopper3 GS3-U3-41C6NIR-C, FLIR, Richmond, BC, Canada) selected for its infrared-enhanced CMOS sensor and global shutter. The system was designed using three wavelengths (920, 940 and 960 nm) with relative weights modeling the LED spectral profile provided by the manufacturer (Marubeni).

Table 3. Fundus imaging lens specifications

Specification	Value
F/#	6.4
Full field of view	12.2° (32° of visual angle)
Focal length	46.6 mm
Spectral bandwidth	920, 940 & 960 nm (relative weights 1, 2 & 1)
Working distance	≥ 10 mm
Overall length	< 100 mm
Aperture stop diameter	2.9 mm at the eye
Performance of all field angles & wavelengths	< $\lambda/14$ RMS wavefront at 0D focus < $\lambda/10$ RMS wavefront as-built at 0D focus < $\lambda/10$ RMS wavefront from -20 to +10D
Aberration correction	Afocal relay aberrations should be compensated
Camera sensor size	11.3 × 11.3 mm (5.5 μ m pixel pitch)
Sensor sampling	182 pix/mm (91 lp/mm, 74 lp/deg @ eye)

A double Gauss lens was selected as the starting solution for the optimization, based on the desired numerical aperture (NA) and FOV [62]. This design was then modified to minimize the RMS wavefront of the combined eye, afocal relay and fundus objective lens, with constraints based on manufacturing considerations, yielding the solution shown in Fig. 4. The performance of this sub-system on its own is limited by field curvature, similar to the afocal relay, resulting in a maximum RMS wavefront of 0.12 waves ($\lambda/8$) over the entire field of view. In order to facilitate testing and assembly, diffraction-limited performance on axis was forced, reaching 0.007 waves ($\lambda/143$) of RMS wavefront.

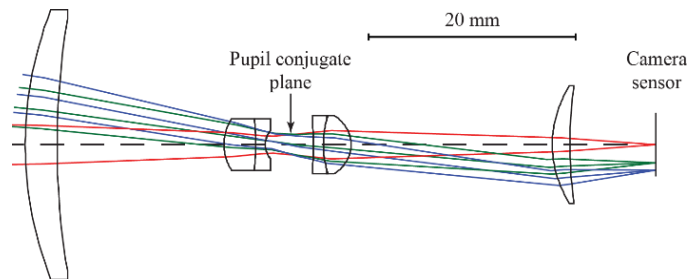


Fig. 4. Fundus objective double Gauss lens layout with a working distance of 14 mm.

The complete fundus imaging system (Fig. 5(a)) has a field curvature more than seven times lower than the fundus objective subsystem, but at the expense of doubling image distortion. This distortion can be corrected digitally by adequate image scaling, and thus, is only monitored to prevent resolution loss or vignetting. The full system has diffraction limited performance with a maximum RMS wavefront of 0.018 waves ($\lambda/56$) and is limited by spherical aberration. The system was optimized at 0D of sphere afocal system focus, resulting in a RMS wavefront of 0.094 and 0.133 waves at -20 and +10D, respectively.

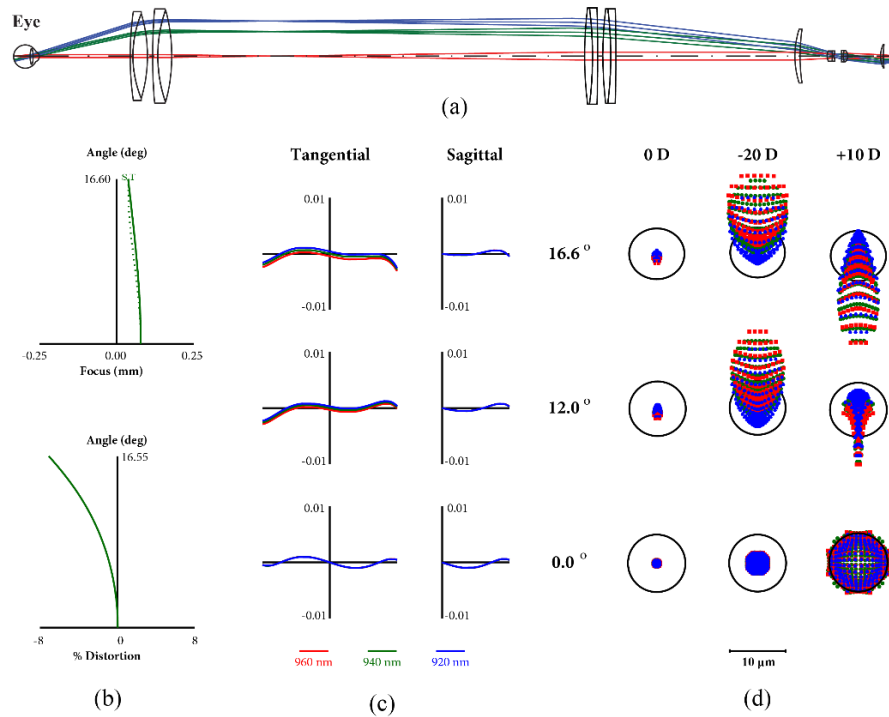


Fig. 5. Afocal relay and fundus objective lens (a) layout, (b) ray curves, (c) field curves and (d) distortion. In the spot diagrams the black circle represents the Airy disk at 940 nm. The scale bar corresponds to the spot diagrams.

Code V's TOR feature was used to perform a tolerance study of lens manufacturing and mechanical assembly errors as per Tables 4 and 5, to predict the cumulative probability that the fully assembled system would have a desired RMS wavefront, The resulting curves (Fig. 6) suggest that better than $\lambda/10$ RMS wavefront can be achieved for all three fields with a greater than 90% yield, with only the camera sensor distance allowed to vary as a correcting method. The balancing of the aberrations generated by the doublets results in tight tolerances that were at the limit of common low cost mounting and alignment techniques. The optical elements for this subsystem, described in Appendix B, were manufactured by Optimax Systems Inc. (Ontario, NY, USA).

Table 4. Afocal relay and fundus imaging lens optical tolerances

Group	Surface	Radius (%)	Thickness (μm)	Wedge TIR* (μm)	Irregularity (waves)	Material (Index, Abbe #)
Afocal relay	1-3	0.2/0.2/0.2	200/200	25/25	1.5/1.5/1.0	0.001, 0.8%
	4-6	0.2/0.2/0.2	200/200	25/26	2.0/2.0/.20	0.001, 0.8%
	7-9	0.2/0.2/0.2	200/200	26/26	2.0/2.0/.20	0.001, 0.8%
	10-12	0.2/0.2/0.2	200/200	26/26	2.0/2.0/.20	0.001, 0.8%
Fundus imaging lens	1-2	0.05/0.24	30	5	0.6/0.6	0.0005, 0.5%
	3-5	0.15/0.17/0.25	20/20	3/3	0.9/0.5/0.5	0.0005, 0.5%
	6-9	0.24/0.13/0.18	22/25	3/4	0.4/0.5/0.5	0.0005, 0.5%
	10-11	0.25/0.25	25	4	0.8/0.4	0.0005, 0.5%

* TIR is wedge as measured by total indicated runout.

Table 5. Afocal relay and fundus imaging lens opto-mechanical tolerances

Group	Element	Diameter (μm)	Element to element roll (μm)	Airspace (μm)	Decenter (μm)	Tilt (arcmin)
Afocal relay	1	+0/-50	25	100	100	5
	2	+0/-100	25	100	100	5
	3	+0/-50	25	100	100	5
	4	+0/-100	25	100	100	5
Fundus imaging lens	1	+0/-10	-	100	100	3
	2	+0/-10	15	30	25	3
	3	+0/-30	25	100	25	3
	4	+0/-20	-	-	100	3

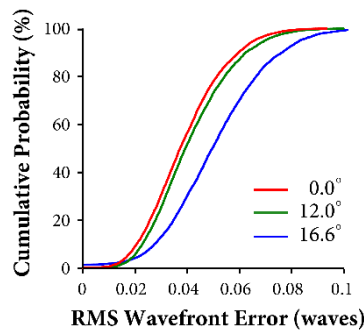


Fig. 6. Afocal relay and fundus objective manufacturing yield of polychromatic (920-960 nm) RMS wavefront error, simulated using 5,000 trials in the TOR sensitivity analysis (Code V).

2.7 Fixation target objective design

In order to achieve more relaxed manufacturing and assembly tolerances than those of the fundus camera objective, the fixation target pupil at the eye was set to 1.5 mm. This smaller pupil provides the additional benefit of reducing the maximum power that the projector could deliver to the eye, which is one or two orders of magnitude more than what is needed for fixation. Table 6 below shows the full set of desired specification.

Table 6. Fixation objective lens specifications

Specification	Value
F/#	4.5
Full field of view	12.2° (32.2° @ eye)
Focal length	17.9 mm
Spectral bandwidth	455, 525, & 625 nm (equal relative weights)
Working distance	> 25 mm
Working distance to prism	> 3.5 mm (see Fig. 7)
Telecentricity	< 1°
Performance at all field angles & wavelengths	< $\lambda/14$ RMS wavefront @ 0 D < $\lambda/10$ RMS wavefront as-built @ 0 D < $\lambda/14$ RMS wavefront from -20 to +10 D
Ocular aberration correction	The residual aberrations from the afocal relay should be corrected.
Light Source	Texas Instruments DLP LightCrafter Display 3010 EVM
DMD	0.3 720p 6.9 x 3.9 mm (5.4 μm micro-mirror pitch)

Digital projectors based on the DMD technology by Texas Instruments Inc. (Dallas, Texas, USA) typically have a glass prism to compactly guide light from the illuminating LEDs first to the micro-mirror array (image plane) and then to the projector lens, introducing

LCA among other aberrations. We selected the Digital Light Projector (DLP) EVM3010DLP due to its compact size and because the manufacturer shared the prism specifications through a non-disclosure agreement, thus allowing us to account for aberrations introduced by the prism. The size of the micro-mirror array, 6.9 by 3.9 mm, dictated that the focal length of the fixation target objective that would couple light into the afocal telescope should be 17.9 mm. Furthermore, telecentricity of the light after the projection lens is required to relay the uniform illumination reaching the micro-mirror array onto the retina. The blue, red and green LEDs used in the DLP were modeled as the LE B Q8WP (455 nm), LE T Q8WP (525 nm), and LE R Q8WP (625 nm) LEDs by Osram (Munich, Germany).

A custom optimization approach, derived from that by Rogers [63], was pursued for the design of this objective lens, in which global solutions were filtered according to their sensitivity to manufacturing tolerances as follows:

1. Choose the number of elements in the starting solution, including the desired focal length, NA & FOV.
2. Run global optimization with sensitivity constraints, performing the following steps on each of the retrieved solutions:
 - a. Replace fictitious materials with real materials from a custom glass catalog.
 - b. Load desired tolerances (see Table 7 below) from a user-defined text file.
 - c. Check if any two adjacent surfaces are close and have similar curvatures. If so, consider cementing if performance is comparable or better.
 - d. Run sensitivity analysis and keep solutions that meet as-built RMS wavefront criterion.
 - e. Optimize (real) materials.
3. Repeat step 1 by changing the number of elements in the starting solution.
4. Rank solutions based on as-built performance and select best.

Table 7. Fixation target optical and opto-mechanical tolerances

Element	Radius (%)	Diameter (um)	Material (index, Abbe #)	Irreg. (waves)	Decenter (um)	Tilt (arcmin)	Wedge TIR (um)	Thickness (um)	Airspace (um)
1	0.25/0.0	+0/-10	0.001, 0.8%	1.5/1.5	25	10.3	20	100	70
2	1.5/1.0	+0/-10	0.001, 0.8%	1.0/1.0	25	4.1	10	100	50
3	1.0/0.23	+0/-10	0.001, 0.8%	1.0/1.0	25	6.9	25	100	70
4	3.7/0.0	+0/-10	0.001, 0.8%	1.0/1.0	25	8.6	20	100	N/A

Three, four and five single-element starting solutions were considered as part of a complete fixation system that included the model eye (see section 2.3), afocal relay, and dichroic mirrors. The system was modeled by starting the ray tracing at the eye and ending it at the DLP micro-mirror array surface. As mentioned above, TCA was ignored to increase the design space. Seven system configurations, using three field of view points (0, 12 & 16.6°) and the three LED wavelengths were used for the optimization process: 1) all three wavelengths on-axis, to correct for all on-axis aberrations including polychromatic aberrations, primarily LCA; 2-7) one per wavelength at each of the two remaining field points (12 & 16.6°), in order to correct the monochromatic aberrations across the field for each wavelength. With the information provided by the manufacturer, the DLP prism and micro-mirror array cover plate were modeled as unfolded pieces of glass. A four-element solution was found to provide the simplest design with the desired as-built performance using common glasses and spherical surfaces. This solution, shown in Fig. 7 (see Appendix B for full system details), consists of two plano-convex lenses, one meniscus lens, and one bi-concave lens. This custom objective was made as a full sub-assembly by Shanghai Optics (Nanjing, China).

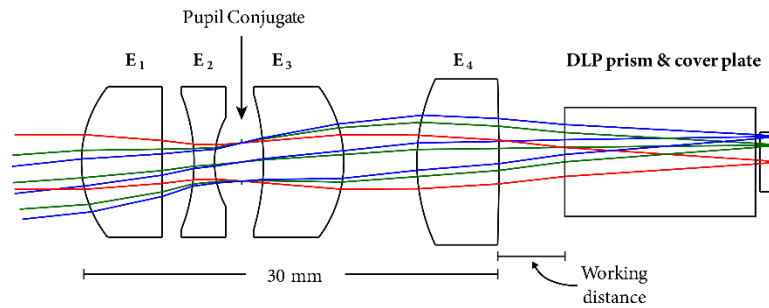


Fig. 7. Fixation target objective layout with a working distance of 4.8 mm and total lens objective length of 30 mm. The DLP prism is shown as a thick piece of glass and includes a cover plate.

The full fixation optical path is dominated by TCA, shown in Fig. 8, but when ignored, is limited by secondary longitudinal chromatic aberration. The monochromatic performance, on the other hand, is diffraction limited and geometrically limited by spherical aberration on-axis and higher-order aberrations off-axis. The maximum RMS wavefront values at 455, 525 and 625 nm are 0.029, 0.029 and 0.025 waves, respectively, when focused at 525 nm. Performance does not change significantly over the 30 D prescription range, with an RMS wavefront at 525 nm of 0.023 and 0.039 waves at -20 and +10 D, respectively. As with the fundus imaging lens, the sensitivity tolerance analysis (TOR, Code V) was run using RMS wavefront error as the metric for 5000 trials. The distance between the last optical element and the DLP was the only variable used as a compensator. The result, shown in Fig. 8 (right), shows that a better than $\lambda/10$ performance would be achieved for 90% of assembled objective lenses at all wavelengths.

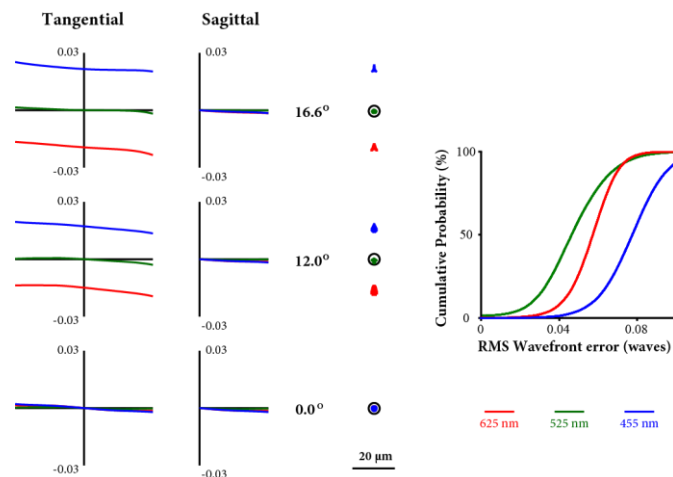


Fig. 8. Fixation objective polychromatic ray curves (left), spot diagram (middle; black circle represents the Airy disk at 525 nm) and simulated manufacturing yield for the worst of the three fields at each wavelength of the complete system with the model eye, excluding TCA (right).

2.8 Mechanical design and alignment

The design of all mechanical parts except the illumination mechanics was outsourced to MoonDog Optics (Fairport, New York, USA). A computer-aided design cross-sectional view of system is shown below in Fig. 9, next to a picture of the real, fully-assembled system. In it, the vertical translation of the highlighted components is achieved with a motorized linear stage MA4030W1-S4 with 25" travel (Velmex Inc., Bloomfield, NY, USA), capable of

providing focus correction, between -25 and $+20$ D over a 22" translation range. The relationship between translation and prescription correction is linear [48]. The part of the system that moves is made compact through the use of a folding mirror. In the imaging arm, the size of the aperture stop can be reduced whenever the subject's astigmatism and/or high-order aberrations result in unacceptable image blur. The LED ring that provides illumination for the fundus camera was centered and focused at the eye's pupil. Then, the linear polarizer adjacent to the LED ring was rotated to minimize internal reflections seen by the camera, which also results in the maximization of the light delivered to the eye. The fundus camera was focused using a model eye with the nominal afocal relay separation (i.e., 0 D of sphere). Because the opto-mechanics did not allow the external rotation of the linear polarizer in front of the sensor, the camera (to which the polarizer was rigidly attached) was rotated to minimize the lens back-reflections. Finally, the fixation target was focused on the retinal plane using the 525 nm channel with a plano-convex lens, (LA1540-A by Thorlabs) to coarsely match the LCA of the human eye. All sub-systems and the AO ophthalmoscope were co-aligned in the pupil and image planes.

3. Results

3.1 Fundus camera objective

The modulation transfer function (MTF) and focal length of the fundus camera objective were measured by Optikos Corp. (Wakefield, MA, USA) in three of the 12 units built. Only the objective lens, as opposed to the full system, was tested due to cost. The average MTF curves, shown in Fig. 10 next to the nominal design ones, were generated by averaging measurements at two locations per off-axis field point of all three tested units. The worst-performing objective showed 30% reduction in on-axis performance as compared to the other two objectives, most likely due to poor assembly. On average, contrast was reduced by ~ 0.2 at the Nyquist frequency of the camera sensor on axis and at 4° . The measured focal length was 45.8 ± 0.2 mm, which is within 2% of the specified 46.6 mm.

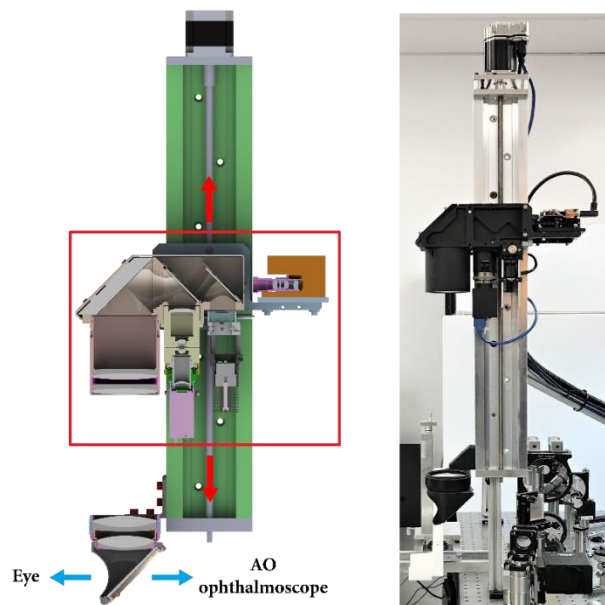


Fig. 9. Instrument cross-section (left), and actual setup integrated with a reflective adaptive optics scanning ophthalmoscope (right). The red arrows indicate translation to correct for focus.

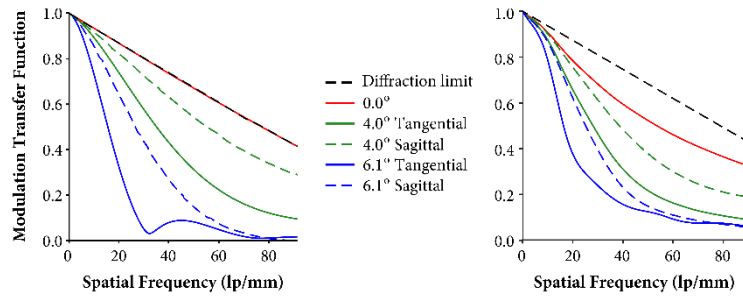


Fig. 10. Fundus camera theoretical (left) and 3-unit average measured modulation transfer function (right), plotted out to the camera's Nyquist frequency (91 lp/mm).

3.2 Complete fundus camera system

The correction of sphere in the complete fundus imaging system was tested using a USAF target (Thorlabs R1DS1P) in the back focal plane of an achromatic doublet (Thorlabs AC254-045-B), placed a focal length away from the camera pupil plane to achieve telecentricity. The target was back-illuminated with 940 nm light with a piece of paper against the back of the target as a diffuser. This diffuse back-illumination coarsely mimics the scattering that we expect from a retina. The target was translated axially to replicate varying degrees of spectacle prescription, with the main body of the fundus camera (see Fig. 9) moved as necessary to refocus the target. Figure 11, below, shows group 4 & 5 of the USAF chart to illustrate the limiting elements of the resolution. Using the USAF target and scaling for the focal length of the lens in the model eye, the contrast near the sensor half-Nyquist sampling (43.2 lp/mm) is comparable over a range of +10 to -20 D of sphere correction.

Image distortion was measured as -3.7% distortion at 12.5° as compared to the nominal -3.9%, by using a grid (Thorlabs R1L3S3P) at the back focal plane of a model eye made by an achromatic doublet (Thorlabs AC254-030-B) for a sphere correction of 0 D.

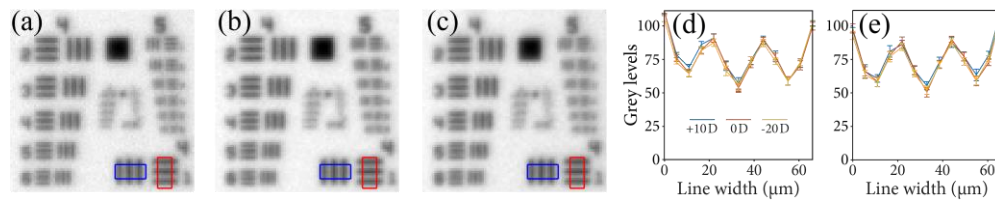


Fig. 11. Image of back-illuminated USAF 1951 target at (a) +10D (b) 0D and (c) -20D using the fundus camera with the blue and red boxes showing the areas for the horizontal and vertical evaluation and the average of seven (d) horizontal and seven (e) vertical cross-sections. Error bars are the standard deviation.

The camera can be used to create larger views of the retina, as shown in Fig. 12 below. This figure was created by montaging seven images in which the subject fixated at the center and six points at the edge of the FOV. The system's performance varies substantially with wavelength as illustrated by the model and human eye images shown in Fig. 13. The model eye images suffer from strong intensity variations across the FOV due to the coatings of the dichroic elements (dichroic mirror D_1 was removed to improve throughput for light safety) at 690, 780, 850 and 940 nm. This is because the designs of the dichroic element coatings were only optimized for 940 nm light and for a small angular range. The illumination for all wavelengths have the same LED ring geometry described earlier, but replacing the LEDs for the corresponding Marubeni part numbers: SMBB690D-1100-02, SMBB780D-1100-02 and SMBB850D-1100-02. Other than for the 850 nm wavelength, the non-uniform image intensity is not substantial, and thus could be corrected through intensity field-flattening.

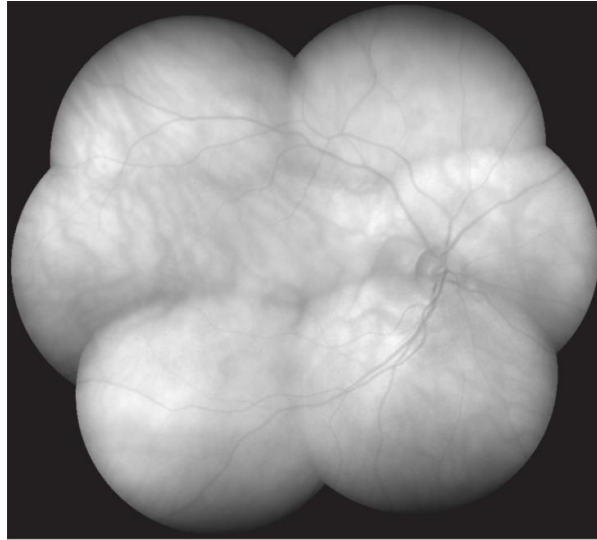


Fig. 12. Contrast-stretched montage of seven fundus images captured 940 nm light in an emmetropic subject (ADS00082), in which each individual image is 32° across.

Lastly, the fixation and fundus imaging system was integrated with an AOSLO [8] and demonstrated as a viewfinder (Fig. 14). The AOSLO images shown here were captured using a 790 nm super-luminescent diode (SLD), delivering an approximate average power of $70 \mu\text{W}$ over a $1.5 \times 1.3^\circ$ field of view (cropped to 1.3° square). The fundus images were captured with 60 ms exposure, to match the AOSLO frame rate, and were processed using ImageJ's CLAHE algorithm [64] to enhance local image contrast, as 940 nm light fundamentally produces lower contrast images of the retina due to its penetration depth.

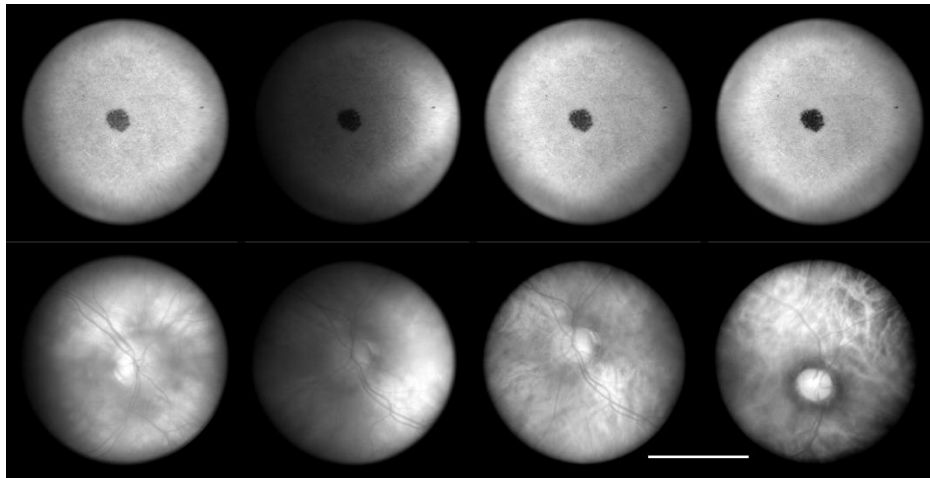


Fig. 13. Images of a model eye (top) and two retinas (subject IDs ADS00054 and ADS00056), using 940, 850, 780 and 690 nm illumination (columns 1-4, respectively). Exposure times were 5, 10, 10 & 15ms, respectively. The black dot in the model eye was used to aid in alignment and focus. The scale bar is 15° .

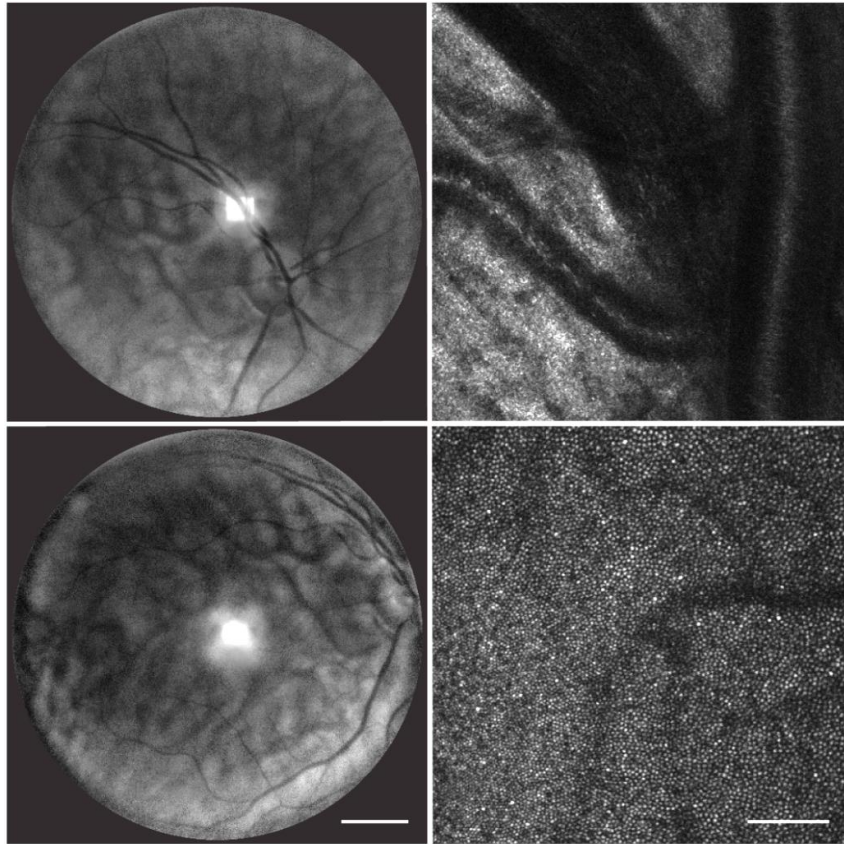


Fig. 14. Demonstration of the fundus camera (left) as the viewfinder of an AO scanning light ophthalmoscope (AOSLO right) at two retinal locations (subject ID ADS00082). The contrast in the fundus images has been enhanced as described in the main text. The scale bars are 5 and 0.25° , respectively.

3.3 Fixation target

Three fixation target objectives were tested by Optikos Corporation, with the average MTF curves plotted below (Fig. 15) with the nominal design MTF provided in the top plots for reference. The measured units have ~ 10 and $\sim 20\%$ lower contrast than the nominal, on- and off-axis, respectively, for all three wavelengths.

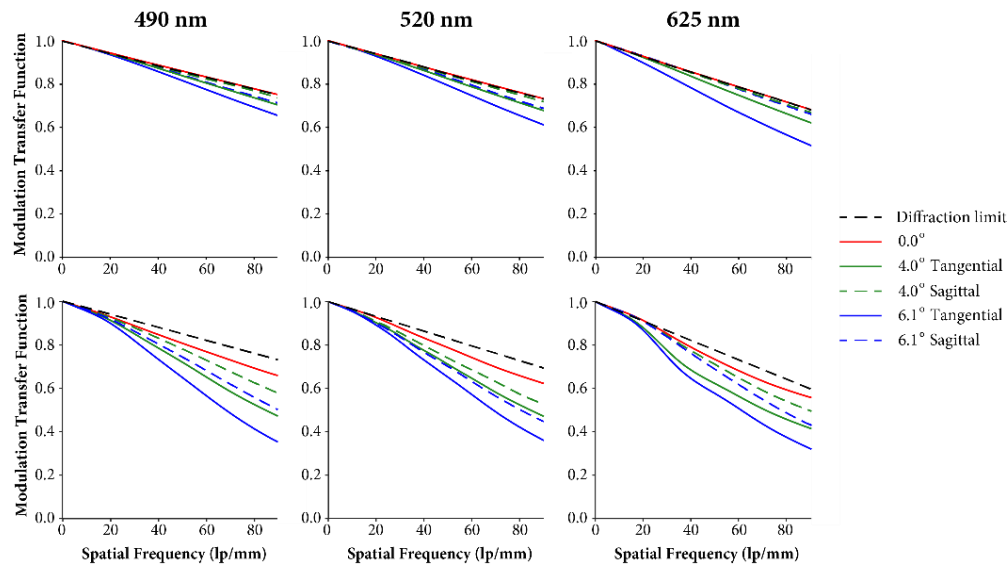


Fig. 15. Fixation target objective lens modulation transfer function: theoretical (top) and average measurement of three units (bottom), tested at 490, 520 and 625 nm. Curves are plotted out to the DMD pixel pitch (90 lp/mm).

The LCA in the fixation arm was measured by displaying a blue, green and red image on the DLP projector, and capturing a stack of images with a monochrome CCD camera and an achromatic doublet (Thorlabs AC254-060-A) as a telecentric focusing lens. This lens has a nominal focal length of 60 mm, 0.002 D of LCA primary color and 0.014 D of secondary color. Each image in the stack corresponds to an approximate 0.09 D axial translation of the camera. The best focus for each color image was then determined based on the contrast between the projector pixels, which were oversampled with the camera pixel array. Table 8 below shows the measured and nominal chromatic focal shifts, as well as those expected from the average human eye [38]. The differences between measured and nominal values are due to optical manufacturing errors, assembly/centering imperfections, and coarse axial sampling. Despite these errors, the LCA in the fixation path was comparable to that of the average human eye, being one fifth (21%) larger, as opposed to the theoretical 5%.

Table 8. Longitudinal shift referenced to 525 nm in the fixation arm in units of diopters

Chromatic shift	455 nm	625 nm	LCA	Secondary color
Average human	-0.59	0.50	1.09	0.59
Design	-0.91	0.23	1.14	0.91
Measured	-1.10	0.22	1.32	1.10

The TCA of the fixation target optical path was measured by sequentially projecting identical red, green and blue patterns with the DLP, onto a monochrome CCD camera with an achromatic doublet (AC127-019-A by Thorlabs) as a focusing lens, using the green image focus as the reference. The difference in height between the blue and red patterns, was measured at four field points, equidistant from the center of the image. In this way, the average measured TCA was 56 μm (0.17°) at 6.9°, which compares well to the theoretical 57 μm (0.17°) accounting for the doublet that focuses the light onto the test camera.

4. Summary

The design and performance of an instrument for near infrared fundus imaging and fixation steering with a long eye relief was presented. The optics was designed to achieve partial correction of the average human LCA and spherical aberration, as well as to correct any

sphere value between -20 and +10 D. In order to meet the desired specifications, including a long eye relief and a 32° full field of view, custom multi-element refractive objectives had to be designed. Sub-systems and a fully assembled instrument were tested, including after integration with an existing AO scanning ophthalmoscope. Fundus images were taken using 12 mW of 940 nm light, ~30 times less than the MPE. The fixation stimulus provides a maximum of 4.2, 12.5 and 6.9 μW for each of the blue, green and red channels, respectively, which is more than two orders of magnitude below the corresponding MPEs.

Appendix A: Maximum permissible exposure calculations

Light safety considerations for the proposed instrument included maximum permissible exposure (MPE) calculations according to the American National Standard Institute “Safe use of lasers Z136.1-2014,” as described next. The LED ring used for illumination in the fundus camera was, for the purpose of the light safety calculations, considered a continuous-wave (CW) extended source that creates uniform illumination over the field of view. The LED nominal central wavelength is 940 nm, with a full-width at half-maximum (FWHM) of 47 nm. To be conservative, we assumed that all the power was delivered at the shortest wavelength of the FWHM bandwidth and that the eye was illuminated for the maximum uninterrupted duration considered by the standard, which is 30,000 s. The safety factor accounting for head restraint (standard section 8.3.2) applies, and thus, a thermal limiting exposure duration of $T_2 = 10^4$ s was used. With these considerations, the MPE calculation only has a thermal component, given by

$$MPE_{fundus\ camera} = 1.8 C_A C_E T_2^{-0.25} mW / cm^2,$$

with $C_A = 10^{0.002(\lambda-700)}$ with the wavelength λ expressed in nm. The factor C_E (892 mW/cm²) captures the angular extent α (visual angle) of the source, which is 30°, which combined with a 7 mm diameter pupil, yields an MPE of 343 mW. This is an order of magnitude higher than the maximum power used at the eye in our test subjects with the shortest (6 ms) camera exposure (30 mW). It is important to note that this is the MPE for the fundus camera on its own, and that when used in combination (simultaneously or not) with other ophthalmoscopes over a 48-hour time window, the MPE should be re-calculated to account for all light exposures.

Each LED in the DLP projector was considered a continuous-wave (CW) extended source that creates uniform illumination over the field of view. The nominal central wavelengths of the LEDs are 455, 525 and 625 nm, with 20 nm spectral FWHMs. To be conservative the MPE was calculated as if all the power was delivered at the shortest wavelength of the FWHM of each LED and assuming that the eye was illuminated for the maximum uninterrupted duration considered by the standard. The safety factors that account for pupil dilation (standard section 8.3.1) and head restraint (standard section 8.3.2) both apply. Section 8.3.1 dictates that the MPE for all three LEDs must be reduced by a factor of 5, while section 8.3.2 indicates a photochemical exposure limit that reduces the MPE value, as well as a change to the thermal MPE calculation. The photochemical limit is calculated by the expression $10 C_B J / sr \cdot cm^2$, or equivalently, $10 C_B \Omega A_{pupil} mW$, where Ω is the solid angle of the source at the pupil. The thermal MPE is calculated with an exposure duration of $T_2 = 10^4$ s. The MPE calculation for the 455 and 525 nm LEDs has both photochemical and thermal component, whereas the 625 nm LED MPE only has a thermal component. The thermal damage component for all three LEDs is given by,

$$MPE_{Thermal} = 0.36 C_E T_2^{-0.25} mW / cm^2,$$

with the angular extent of the source C_E being 892 mW/cm^2 , as for the fundus camera illumination, resulting in the thermal MPE for a 7 mm diameter pupil of 25 mW for each LED. The photochemical damage component is given by,

$$MPE_{\text{Photochemical}} = 2C_B,$$

with $C_B = 1$ for the blue LED and 20 for the red and green LEDs. The solid angle of the source at the eye, should all the projector's pixels be turned on at the same time, is given by $\Omega = 2\pi(1 - \cos\alpha) = 0.2 \text{ sr}$. Thus, assuming a 7 mm diameter pupil, the photochemical MPE for the blue and green LEDs are $165 \mu\text{W}$ and 3.3 mW , respectively. These are lower than the thermal MPE and thus the ones that need to be reported for the blue and green LEDs. Thus, in summary, the MPEs for the blue, green, and red channels of the fixation target are $165 \mu\text{W}$, 3.3 mW and 25 mW , respectively. After inserting a neutral density filter (O.D. 2.0, part # NE20A by Thorlabs) to reduce the maximum potential retinal light exposure, we measured after turning all the pixels on with the maximum brightness: 4.2 , 12.5 and $6.9 \mu\text{W}$ for each of the blue, green and red channels, respectively, which is more than two orders of magnitude below the corresponding MPEs. As with the fundus camera, the MPEs calculated here for each individual LED should be combined if more than one LED is used, and also combined with the MPE of any other ophthalmoscope used over a 48-hour time window.

Appendix B: Lens data

The curvatures, thickness, and materials of every element of the complete optical design are provided in Table 9 below. As per Fig. 1, the afocal relay and the schematic eye are common to the fixation target and fundus imaging arms. The first dichroic (D_1) and the fold mirror are not included here.

Table 9. Fundus and fixation target lens data

Element	Radius (mm)	Thickness (mm)	Diameter (mm)	Material	
Schematic Eye	Infinity	16.67			
	Lens Module	Type:	Not Chromatic		
		Focal Length:	16.67 mm		
		Principal reduction ratio:	1×10^7		
		Front/Rear focal point:	± 16.67 mm		
		Entrance pupil:	0.00 mm		
		Field specification mode:	Degrees		
		Field value:	16.6°		
		Entrance Pupil Diameter:	2.5 mm		
		Wavelengths:	Fundus: 960, 940 & 920 nm		
		Axial Color:	Fixation: 625, 587.6 & 455 nm		
Lateral Color:	Fundus: $-0.9745, -0.9515, -0.927 \lambda$				
	Fixation: $-0.0753, 0.0, 0.446 \lambda$				
Fringe Zernike Surface	Fundus: $0.0151, 0, -0.161 \lambda$				
	Fixation: $0.1190, 0.0, -0.7047 \lambda$				
Afocal Relay	Infinity	0	Normalized radius: 2.85 mm $C12 = -6.17 \times 10^{-5}$ mm		
	1	260.01	2.6	66.0	N-SF5
		89.89	14.0	66.0	N-BK7
		-119.63	5.0	66.0	
	2	431.76	5.0	75.0	N-SF2
		112.84	13.5	75.0	N-BK7
		-140.36	396.6	75.0	
	3	309.44	7.6	76.2	N-BK7
		-309.44	5.0	76.2	N-SF5
		-1339.71	5.0	76.2	
	4	309.44	7.6	76.2	N-BK7
		-309.44	5.0	76.2	N-SF5
		-1339.71		76.2	
	Fundus Camera		190.46	-	
		1	52.50	5.00	30.0
211.81			31.49	30.0	
2		9.79	4.97	9.76	N-PK51
		-17.18	1.51	9.76	N-KZFS11
		4.07	2.86	9.86 (sag = 1.36)	
Aperture stop		1.66	3.6		
3		-32.83	1.51	8.68 (sag = 0.16)	N-KZFS11
		19.73	4.33	8.57	S-FPL53
		-6.02	32.50	8.57	
4		15.70	2.74	17.9	TAFD30
		34.32	14.90	17.9	
Fixation Target		170.46			
	D ₂	Infinity	2.09	55.0	N-BK7
		Infinity	45.00	55.0	
	D ₃	Infinity	2.09	55.0	N-BK7
		Infinity	50.75	55.0	
	1	8.82	5.90	10.0	H-FK61
		Infinity	2.34	10.0	
	2	-13.55	1.50	10.0 (sag = 0.81)	ZF2
		6.84	2.00	10.0 (sag = 0.24)	
	Aperture Stop		1.58	2.8	
	3	-17.46	5.88	10.0 (sag = 0.55)	H-ZPK1
		-9.17	5.35	10.0	
	4	14.30	6.00	11.0	H-LAK52
		-185.20	20.5	11.0	Mixed (TI confidential)

Funding

Glaucoma Research Foundation Catalyst for a Cure Initiative; Research to Prevent Blindness Departmental Challenge Award (Stanford); National Eye Institute of the National Institutes of Health (P30 EY026877, U01 EY025477, R01 EY028287 and R01 EY025231); Kleberg Foundation.

Acknowledgements

We would like to thank Nripun Sredar, Moataz Razeen, and Vyas Akondi for assistance with data collection, as well as Bartłomiej Kowalski and Mike Han for help with custom image acquisition software. We would also like to thank Steve Shaw and Gavin Perrella of Texas Instruments DLP systems group as well as the Pico business unit for their donation of DLP units and their provision of the reference design for the projector.

Disclosures

The authors declare that there are no conflicts of interest related to this article.

References

1. J. Liang, D. R. Williams, and D. T. Miller, "Supernormal vision and high-resolution retinal imaging through adaptive optics," *J. Opt. Soc. Am. A* **14**(11), 2884–2892 (1997).
2. A. Roorda, F. Romero-Borja, W. Donnelly Iii, H. Queener, T. Hebert, and M. Campbell, "Adaptive optics scanning laser ophthalmoscopy," *Opt. Express* **10**(9), 405–412 (2002).
3. D. T. Miller, J. Qu, R. S. Jonnal, and K. Thorn, "Coherence gating and adaptive optics in the eye," *Proc. SPIE* **4956**, 65–72 (2003).
4. E. J. Fernández, B. Považay, B. Hermann, A. Unterhuber, H. Sattmann, P. M. Prieto, R. Leitgeb, P. Ahnelt, P. Artal, and W. Drexler, "Three-dimensional adaptive optics ultrahigh-resolution optical coherence tomography using a liquid crystal spatial light modulator," *Vision Res.* **45**(28), 3432–3444 (2005).
5. D. X. Hammer, R. D. Ferguson, C. E. Bigelow, N. V. Iftimia, T. E. Ustun, and S. A. Burns, "Adaptive optics scanning laser ophthalmoscope for stabilized retinal imaging," *Opt. Express* **14**(8), 3354–3367 (2006).
6. M. Pircher, R. J. Zawadzki, J. W. Evans, J. S. Werner, and C. K. Hitzenberger, "Simultaneous imaging of human cone mosaic with adaptive optics enhanced scanning laser ophthalmoscopy and high-speed transversal scanning optical coherence tomography," *Opt. Lett.* **33**(1), 22–24 (2008).
7. R. J. Zawadzki, S. S. Choi, A. R. Fuller, J. W. Evans, B. Hamann, and J. S. Werner, "Cellular resolution volumetric in vivo retinal imaging with adaptive optics-optical coherence tomography," *Opt. Express* **17**(5), 4084–4094 (2009).
8. A. Dubra and Y. Sulai, "Reflective afocal broadband adaptive optics scanning ophthalmoscope," *Biomed. Opt. Express* **2**(6), 1757–1768 (2011).
9. H. Hofer, N. Sredar, H. Queener, C. Li, and J. Porter, "Wavefront sensorless adaptive optics ophthalmoscopy in the human eye," *Opt. Express* **19**(15), 14160–14171 (2011).
10. J. A. Feeks and J. J. Hunter, "Adaptive optics two-photon excited fluorescence lifetime imaging ophthalmoscopy of exogenous fluorophores in mice," *Biomed. Opt. Express* **8**(5), 2483–2495 (2017).
11. L. Mariotti, N. Devaney, G. Lombardo, and M. Lombardo, "Understanding the changes of cone reflectance in adaptive optics flood illumination retinal images over three years," *Biomed. Opt. Express* **7**(7), 2807–2822 (2016).
12. M. Mujat, A. Patel, N. Iftimia, and R. D. Ferguson, "Compact adaptive optics line scanning retinal imager; closer to the clinic," *Proc. SPIE* **8930**, 89301B (2014).
13. F. Hirose, K. Nozato, K.-i. Saito, and Y. Numajiri, "A compact adaptive optics scanning laser ophthalmoscope with high-efficiency wavefront correction using dual liquid crystal on silicon - spatial light modulator," *Proc. SPIE* **7885**, 788515 (2011).
14. A. T. Sheyman, P. L. Nesper, A. A. Fawzi, and L. M. Jampol, "Adaptive Optics Imaging in Laser Pointer Maculopathy," *Ophthalmic Surg. Lasers Imaging Retina* **47**(8), 782–785 (2016).
15. P. Bedgood, M. Daaboul, R. Ashman, G. Smith, and A. Metha, "Characteristics of the human isoplanatic patch and implications for adaptive optics retinal imaging," *J. Biomed. Opt.* **13**(2), 024008 (2008).
16. M. Nowakowski, M. Sheehan, D. Neal, and A. V. Goncharov, "Investigation of the isoplanatic patch and wavefront aberration along the pupillary axis compared to the line of sight in the eye," *Biomed. Opt. Express* **3**(2), 240–258 (2012).
17. R. D. Ferguson, Z. Zhong, D. X. Hammer, M. Mujat, A. H. Patel, C. Deng, W. Zou, and S. A. Burns, "Adaptive optics scanning laser ophthalmoscope with integrated wide-field retinal imaging and tracking," *J. Opt. Soc. Am. A* **27**(11), A265–A277 (2010).
18. J. Zhang, Q. Yang, K. Saito, K. Nozato, D. R. Williams, and E. A. Rossi, "An adaptive optics imaging system designed for clinical use," *Biomed. Opt. Express* **6**(6), 2120–2137 (2015).

19. C. K. Sheehy, P. Tiruveedhula, R. Sabesan, and A. Roorda, "Active eye-tracking for an adaptive optics scanning laser ophthalmoscope," *Biomed. Opt. Express* **6**(7), 2412–2423 (2015).
20. A. Dubra and Y. N. Sulai, "First-order design of a reflective viewfinder for adaptive optics ophthalmoscopy," *Opt. Express* **20**(24), 26596–26605 (2012).
21. G. Y. Yoon and D. R. Williams, "Visual performance after correcting the monochromatic and chromatic aberrations of the eye," *J. Opt. Soc. Am. A* **19**(2), 266–275 (2002).
22. J. Rha, R. S. Jonnal, K. E. Thorn, J. Qu, Y. Zhang, and D. T. Miller, "Adaptive optics flood-illumination camera for high speed retinal imaging," *Opt. Express* **14**(10), 4552–4569 (2006).
23. A. Roorda, Y. Zhang, and J. L. Duncan, "High-resolution in vivo imaging of the RPE mosaic in eyes with retinal disease," *Invest. Ophthalmol. Vis. Sci.* **48**(5), 2297–2303 (2007).
24. S. Li, Y. Xiong, J. Li, N. Wang, Y. Dai, L. Xue, H. Zhao, W. Jiang, Y. Zhang, and J. C. He, "Effects of monochromatic aberration on visual acuity using adaptive optics," *Optom. Vis. Sci.* **86**(7), 868–874 (2009).
25. H. Hofer, L. Chen, G. Y. Yoon, B. Singer, Y. Yamauchi, and D. R. Williams, "Improvement in retinal image quality with dynamic correction of the eye's aberrations," *Opt. Express* **8**(11), 631–643 (2001).
26. Y. Zhang, J. Rha, R. Jonnal, and D. Miller, "Adaptive optics parallel spectral domain optical coherence tomography for imaging the living retina," *Opt. Express* **13**(12), 4792–4811 (2005).
27. R. J. Zawadzki, S. M. Jones, S. S. Olivier, M. Zhao, B. A. Bower, J. A. Izatt, S. Choi, S. Laut, and J. S. Werner, "Adaptive-optics optical coherence tomography for high-resolution and high-speed 3D retinal in vivo imaging," *Opt. Express* **13**(21), 8532–8546 (2005).
28. D. Merino, C. Dainty, A. Bradu, and A. G. Podoleanu, "Adaptive optics enhanced simultaneous *en-face* optical coherence tomography and scanning laser ophthalmoscopy," *Opt. Express* **14**(8), 3345–3353 (2006).
29. D. X. Hammer, R. D. Ferguson, C. E. Bigelow, N. V. Iftimia, T. E. Ustun, and S. A. Burns, "Adaptive optics scanning laser ophthalmoscope for stabilized retinal imaging," *Opt. Express* **14**(8), 3354–3367 (2006).
30. C. E. Bigelow, N. V. Iftimia, R. D. Ferguson, T. E. Ustun, B. Bloom, and D. X. Hammer, "Compact multimodal adaptive-optics spectral-domain optical coherence tomography instrument for retinal imaging," *J. Opt. Soc. Am. A* **24**(5), 1327–1336 (2007).
31. R. S. Jonnal, J. Rha, Y. Zhang, B. Cense, W. Gao, and D. T. Miller, "In vivo functional imaging of human cone photoreceptors," *Opt. Express* **15**(24), 16141–16160 (2007).
32. C. Torti, B. Považay, B. Hofer, A. Unterhuber, J. Carroll, P. K. Ahnelt, and W. Drexler, "Adaptive optics optical coherence tomography at 120,000 depth scans/s for non-invasive cellular phenotyping of the living human retina," *Opt. Express* **17**(22), 19382–19400 (2009).
33. H. Li, J. Lu, G. Shi, and Y. Zhang, "Automatic montage of retinal images in adaptive optics confocal scanning laser ophthalmoscope," *Opt Eng* **51**(5), 057008 (2012).
34. M. Chen, R. F. Cooper, G. K. Han, J. Gee, D. H. Brainard, and J. I. Morgan, "Multi-modal automatic montaging of adaptive optics retinal images," *Biomed. Opt. Express* **7**(12), 4899–4918 (2016).
35. B. Davidson, A. Kalitzeos, J. Carroll, A. Dubra, S. Ourselin, M. Michaelides, and C. Bergeles, "Fast adaptive optics scanning light ophthalmoscope retinal montaging," *Biomed. Opt. Express* **9**(9), 4317–4328 (2018).
36. I. Newton, *Opticks (1730)*, fourth ed. (Reprinted by Bell, London, 1931).
37. L. N. Thibos, A. Bradley, D. L. Still, X. Zhang, and P. A. Howarth, "Theory and measurement of ocular chromatic aberration," *Vision Res.* **30**(1), 33–49 (1990).
38. L. N. Thibos, M. Ye, X. Zhang, and A. Bradley, "The chromatic eye: A new reduced-eye model of ocular chromatic aberration in humans," *Appl. Opt.* **31**(19), 3594–3600 (1992).
39. E. Fernández, A. Unterhuber, P. Prieto, B. Hermann, W. Drexler, and P. Artal, "Ocular aberrations as a function of wavelength in the near infrared measured with a femtosecond laser," *Opt. Express* **13**(2), 400–409 (2005).
40. W. M. Harmening, P. Tiruveedhula, A. Roorda, and L. C. Sincich, "Measurement and correction of transverse chromatic offsets for multi-wavelength retinal microscopy in the living eye," *Biomed. Opt. Express* **3**(9), 2066–2077 (2012).
41. H. C. Howland and B. Howland, "A subjective method for the measurement of monochromatic aberrations of the eye," *J. Opt. Soc. Am.* **67**(11), 1508–1518 (1977).
42. J. Porter, A. Guirao, I. G. Cox, and D. R. Williams, "Monochromatic aberrations of the human eye in a large population," *J. Opt. Soc. Am. A* **18**(8), 1793–1803 (2001).
43. L. N. Thibos, X. Hong, A. Bradley, and X. Cheng, "Statistical variation of aberration structure and image quality in a normal population of healthy eyes," *J. Opt. Soc. Am. A* **19**(12), 2329–2348 (2002).
44. H.-M. Wu, B. Seet, E. P.-H. Yap, S.-M. Saw, T.-H. Lim, and K.-S. Chia, "Does Education Explain Ethnic Differences in Myopia Prevalence? A Population-Based Study of Young Adult Males in Singapore," *Optom. Vis. Sci.* **78**(4), 234–239 (2001).
45. R. R. A. Bourne, B. P. Dineen, S. M. Ali, D. M. Noorul Huq, and G. J. Johnson, "Prevalence of refractive error in Bangladeshi adults: results of the National Blindness and Low Vision Survey of Bangladesh," *Ophthalmology* **111**(6), 1150–1160 (2004).
46. C. Wolfram, R. Höhn, U. Kottler, P. Wild, M. Blettner, J. Bühren, N. Pfeiffer, and A. Mirshahi, "Prevalence of refractive errors in the European adult population: the Gutenberg Health Study (GHS)," *Br. J. Ophthalmol.* **98**(7), 857–861 (2014).
47. K. M. Williams, V. J. M. Verhoeven, P. Cumberland, G. Bertelsen, C. Wolfram, G. H. S. Buitendijk, A. Hofman, C. M. van Duijn, J. R. Vingerling, R. W. A. M. Kuijpers, R. Höhn, A. Mirshahi, A. P. Khawaja, R. N. Luben, M. G. Erke, T. von Hanno, O. Mahroo, R. Hogg, C. Gieger, A. Cougnard-Grégoire, E. Anastasopoulos,

- A. Bron, J.-F. Dartigues, J.-F. Korobelnik, C. Creuzot-Garcher, F. Topouzis, C. Delcourt, J. Rahi, T. Meitinger, A. Fletcher, P. J. Foster, N. Pfeiffer, C. C. W. Klaver, and C. J. Hammond, "Prevalence of refractive error in Europe: the European Eye Epidemiology (E(3)) Consortium," *Eur. J. Epidemiol.* **30**(4), 305–315 (2015).
48. G. Smith and D. A. Atchison, *The Eye and Visual Optical Instruments* (Cambridge University Press, New York, 1997).
49. J. J. Vos, "Colormetric and photometric properties of a 2 degree fundamental observer," *Color Res. Appl.* **3**(3), 125–128 (1978).
50. J. Rha, B. Schroeder, P. Godara, and J. Carroll, "Variable optical activation of human cone photoreceptors visualized using a short coherence light source," *Opt. Lett.* **34**(24), 3782–3784 (2009).
51. R. F. Cooper, W. S. Tuten, A. Dubra, D. H. Brainard, and J. I. W. Morgan, "Non-invasive assessment of human cone photoreceptor function," *Biomed. Opt. Express* **8**(11), 5098–5112 (2017).
52. G. Michelson, A. Patzelt, and J. Harazny, "Flickering Light Increases Retinal Blood Flow," *Retina* **22**(3), 336–343 (2002).
53. K. Polak, L. Schmetterer, and C. E. Riva, "Influence of Flicker Frequency on Flicker-Induced Changes of Retinal Vessel Diameter," *Invest. Ophthalmol. Vis. Sci.* **43**(8), 2721–2726 (2002).
54. G. T. Dorner, G. Garhöfer, K. H. Huemer, C. E. Riva, M. Wolzt, and L. Schmetterer, "Hyperglycemia affects flicker-induced vasodilation in the retina of healthy subjects," *Vision Res.* **43**(13), 1495–1500 (2003).
55. G. T. Dorner, G. Garhofer, B. Kiss, E. Polska, K. Polak, C. E. Riva, and L. Schmetterer, "Nitric oxide regulates retinal vascular tone in humans," *Am. J. Physiol. Heart Circ. Physiol.* **285**(2), H631–H636 (2003).
56. L. N. Thibos, X. Hong, A. Bradley, and X. Cheng, "Statistical variation of aberration structure and image quality in a normal population of healthy eyes," *J. Opt. Soc. Am. A* **19**(12), 2329–2348 (2002).
57. W. J. Donnelly 3rd and A. Roorda, "Optimal pupil size in the human eye for axial resolution," *J. Opt. Soc. Am. A* **20**(11), 2010–2015 (2003).
58. L. Thibos, R. A. Applegate, J. T. Schwiegerling, and R. Webb, "Standards for reporting the optical aberrations of eyes," in *Vision Science and its Applications*, OSA Technical Digest (Optical Society of America, 2000).
59. A. Bennett and J. Francis, "Retinoscopy and Ophthalmoscopy," in *The Eye: Visual Optics and the Optical Spatial Sense*, H. Davson, ed. (Academic, 1962), pp. 181–208.
60. H. A. Knoll, "Ophthalmic instruments," in *Applied Optics and Optical Engineering, Volume 5, Optical Instruments, Part 2*, R. Kingslake, ed. (Academic, 1969).
61. E. DeHoog and J. Schwiegerling, "Optimal parameters for retinal illumination and imaging in fundus cameras," *Appl. Opt.* **47**(36), 6769–6777 (2008).
62. W. Smith, *Modern Lens Design* (McGraw-Hill Education, 2004).
63. J. Rogers, "Global optimization and desensitization," *Proc. SPIE* **9633**, 96330S (2015).
64. K. Zuiderveld, "Contrast limited adaptive histogram equalization," in *Graphics Gems IV* (Academic Press, 1994).